Research Article Vol. 60, No. 11 / 10 April 2021 / Applied Optics 3081

applied optics

Optimization-free customization of optical tightly focused fields: uniform needles and hotspot chains

Jun He,[1] Jicheng Zhuang,[2] Li Ding,[3] and Kun Huang[1,*]

[1]Department of Optics and Optical Engineering, University of Science and Technology of China, Hefei, Anhui 230026, China
[2]Huangshan Jinggong Gravure Cylinder Co. LTD., No. 8 Wenfeng West Road, Huangshan, Anhui 245900, China
[3]Key Laboratory of Intelligent Computing and Signal Processing of Ministry of Education, School of Electronics and Information Engineering, Anhui University, Hefei, Anhui 230601, China
*Corresponding author: huangk17@ustc.edu.cn

Received 29 December 2020; revised 24 February 2021; accepted 16 March 2021; posted 18 March 2021 (Doc. ID 418415); published 6 April 2021

An optimization-free method based on an inverse problem of nonlinear equations is employed to design the binary phase diffraction optical element (BPDOE) that could modulate the incident light of a high-numerical-aperture (NA) objective lens so that the axisymmetric focal fields can be customized on demand. For example, a 43λ-long optical longitudinally polarized needle with its lateral size beyond diffraction limit is reported by using a 27-belt BPDOE, where the cost evaluated by the ratio of the belt number of BPDOE to the length of needle is record small compared with other optimization algorithms. Moreover, another longitudinal field with multiple hotspots along the propagation direction of light is also achieved with a 10-belt BPDOE. These achieved focal fields are verified doubly by using a finite-difference time-domain (FDTD) method, indicating the validity of Richards–Wolf vector diffraction theory. This optimization-free approach makes the design of BPDOEs with numerous belts viable to generate the expected focal fields, which might benefit various applications such as optical trapping, super-resolution imaging, and lithography.

https://doi.org/10.1364/AO.418415

1. INTRODUCTION

Achieving a focal spot with sub-diffraction size is always a hotspot due to its critical role in applications, such as nanolithography, high-density data storage, super-resolution imaging, and particle manipulation [1–3]. Particularly, a sub-diffraction optical needle (SDON) is more important because it can image three-dimensional nano-objects with an ultrahigh resolution due to the good tolerance to the out-of-focus sample [4]. The current methods to generate such a SDON are categorized into three cases: planar diffractive lenses [4–9], reflective mirrors [10,11] or axicons [12], and high-NA objective lenses with the designed phase or amplitude elements [9–11,13–22]. The planar diffractive lenses with the axisymmetrically arranged micro-/nanostructures realize the SDON by optimizing the locations and optical responses (i.e., phase and amplitude modulation) of structures. Because both functionalities of optical focusing and the extended depth of focus are realized simultaneously in a SDON, the planar diffractive lenses need a large number of belt-like structures and thus increase the complexity of the lens design. Although the planar diffractive lenses can create long (tens of wavelengths) SDONs, the cost (evaluated by the ratio of the belt number to the length of SDON) is extremely high, such as 5.33 belts/λ [4,9] and 127.6 belts/λ [23]. The reflective axicons and mirrors realize the SDONs by making the reflected light overlain at the optical axis for constructive interference. It imposes the rigorous requirement on the curvature and precision of the reflective nonspherical surfaces, which challenge the fabrication. Although the SDONs created by using the reflective devices could have the length from 1000λ [10] to 50, 000λ [12], their working distances are quite limited for practical usage. Consequently, the SDONs created in the reflective configuration are theoretically proposed without any experimental proof.

In contrast, the third method by using the high-NA objective lenses with additional amplitude or phase belts has been paid more attention because only several belts are sufficient to create the SDONs [13–21,24]. Since some structured light such as tightly autofocusing beams [25], symmetric Airy beams [26] and Bessel–Gauss beams [27,28] carry the intrinsic phase and amplitude modulation, their tightly focused fields by a high-NA objective could have a SDON directly without any phase or amplitude elements. However, these reported SDONs have the limited length around 10λ, which is insufficient to characterize high-aspect-ratio objects in imaging and lithography. To extend it, a thin annular of radially polarized Bessel–Gauss light

created by the combination of axcion and simple lens is taken as incident beam to create optical needles [11,22]. However, the transverse full width at half-maximum (FWHM) of optical needle is related to the longitudinal FWHM, resulting in the fact that the transverse FWHM exceeds the diffraction limit with small focusing angles. Up to now, a pure-phase element to create high-efficiency ultralong SDONs has still been absent in the configuration of the high-NA objective, because all the reported methods to design the phase elements have limitations such as the small number of belts or time-cost optimization algorithms.

To solve the problem, here we employ an optimization-free method to design the belt-unlimited binary phase for creating arbitrarily customized focal fields with circular symmetry such as SDONs and optical multifocus chains. This optimization-free approach converts the design of belts into the problem of solving a nonlinear equation numerically by using advanced Newton's theory [29]. Benefitting from it, a 43λ-long SDON is created by using a 27-belt pure-phase element, which thus exhibits much smaller cost of only 0.628 belts/λ. This method is extended to construct the multi-hotspot field near the focal region, suggesting a universal platform to customize the focal fields.

2. PRINCIPLE

As shown in Fig. 1(a), cylindrical vector (CV) beams [30] with spatially variant states of polarization are the axially symmetric beam solution of the full vector electromagnetic wave equation [31], which can be generated in different optical systems [30,32,33]. Recently, the CV beams have attracted the great attention due to their unique properties under high-numerical-aperture (NA) focusing [30,34], excellent performance in dark-field imaging [35], and unusual angular momentum [36,37]. Particularly, the radially polarized [Fig. 1(b)] and azimuthally polarized [Fig. 1(c)] light are the most important to create the longitudinally and transversely polarized SODNs, respectively.

The SODNs can carry the transverse or longitudinal polarization, which depends on the polarization of incident light. The transversely polarized SODNs are easily obtained by using the incident light with linear or circular polarization, azimuthal polarization with a helical phase [38,39], or hybridly polarized vector optical field [40]. But the longitudinal SODNs can only be generated by focusing the radially polarized light by a high-NA lens while chain-like longitudinal field can also be obtained by using radially polarized light [41]. A longitudinal SODNs presents an axially (i.e., the propagation direction z) oscillating dipole, which is usually used in particle acceleration

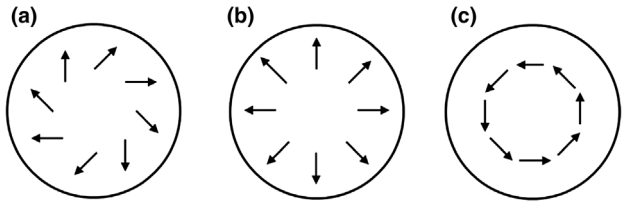

Fig. 1. Spatial distribution of instantaneous electric vector field for CV beams. (a) Generalized CV beams. (b) Radially polarized beam. (c) Azimuthally polarized beam.

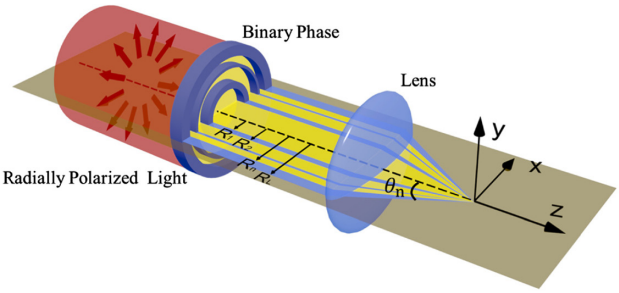

Fig. 2. Schematic of focusing radially polarized light with a high-NA lens and a binary-phase diffractive optical element.

[42], second-harmonic generation [43,44], Raman spectroscopy [45], and high-resolution near-field optical microscopy [46]. Without the loss of generality, we take the creation of the longitudinal SODNs as an example to demonstrate the optimization-free method. Figure 2 sketches the working principle of focusing a radially polarized light by a high-NA objective with a multi-belt phase element. According to Richards and Wolf's vector diffraction (RWVD) theory [30,31,47], the electric fields near the focus plane for a radially polarized incident light can be described as

$$E_r(r,z) = A\int_0^{\theta_{\max}} \sqrt{\cos\theta}\sin(2\theta)\, P(\theta)\, J_1(kr\sin\theta)\, e^{ikz\cos\theta}\mathrm{d}\theta, \tag{1}$$

and

$$E_z(r,z) = 2iA\int_0^{\theta_{\max}} \sqrt{\cos\theta}\sin^2\theta\, P(\theta)\, J_0(kr\sin\theta)\, e^{ikz\cos\theta}\mathrm{d}\theta, \tag{2}$$

where A is a constant, θ denotes the angle between the convergent ray and optical axis, $\theta_{\max} = \arcsin(NA/n)$, the numerical aperture $NA = 0.95$, and the refraction index $n = 1$ in our design, J_0 and J_1 denote the zero- and first-order Bessel functions of the first kind, respectively. The apodization function $P(\theta)$ describing the amplitude of the incident Bessel–Gaussian beam [31] at its waist is given by

$$P(\theta) = J_1\left[2\beta_0\frac{\sin(\theta)}{\sin(\theta_{\max})}\right]\exp\left[-\left(\beta_0\frac{\sin(\theta)}{\sin(\theta_{\max})}\right)^2\right], \tag{3}$$

where $\beta_0 = 1$ is the ratio of pupil radius and the beam waist in our design. To customize the focal fields, a BPDOE consisting of annulus belts with alternating phase of 0 and π is located at the pupil plane of the high-NA objective, and the radius of the outermost belt of BPDOE is same as R_L of the high-NA lens as shown in Fig. 1. Thus, the apodization function $P(\theta)$ in Eqs. (1) and (2) is replaced by $P(\theta)T(\theta)$, where $T(\theta) = \exp[i\phi(\theta)]$ is the transmission function of the BPDOE. Due to the alternating phase (0 and π) of belts, $T(\theta)$ is written as

$$T(\theta) = \begin{cases} 1, & \theta_{n-1} < \theta < \theta_n \\ -1, & \theta_{n-2} < \theta < \theta_{n-1} \end{cases}. \tag{4}$$

After replacing $P(\theta)$ with $P(\theta)T(\theta)$ in Eqs. (1) and (2), the on-axis field by setting $r = 0$ contains only the longitudinal component and is expressed as

$$U(\mathrm{z}) = \sum_{n=1}^{N} (-1)^n \cdot 2iA \int_{\theta_{n-1}}^{\theta_n} P(\theta)\, e^{ikz\cos(\theta)} \sin(\theta)\, \mathrm{d}\theta$$

$$= \sum_{n=1}^{N} (-1)^n \cdot u_n(z), \tag{5}$$

which helps us to customize the axial intensity. The electric field in Eq. (5) mainly depends on $\theta_n = \arcsin(\sin\theta_{\max} R_n / R_L)$ and z, where R_n is the radius of the nth belt (see Fig. 1) and $\sin\theta_{\max} = 0.95$ for the 0.95 NA objective lens. We define the amplitude coefficient $C_n = (-1)^n u_n(0)$ that represents the focal field contributed by the nth belt and the normalized amplitude $D_n = u_n(z)/u_n(0)$ [48]. Finally, we have the on-axis electric field

$$U(\mathrm{z}) = \sum_{n=1}^{N} C_n \cdot D_n. \tag{6}$$

To realize the intensity $\mathbf{I} = [I_1, I_2, \ldots, I_m]^T$ at the predefined position $\mathbf{z} = [z_1, z_2, \ldots, z_m]^T$ (where the sign T means the transpose of a matrix), we need to solve a nonlinear equation [48]

$$\begin{pmatrix} D_1(z_1) & \cdots & D_n(z_1) \\ \vdots & \ddots & \vdots \\ D_1(z_m) & \cdots & D_n(z_m) \end{pmatrix} \begin{pmatrix} C_1 \\ \vdots \\ \mathrm{C_n} \end{pmatrix} = \begin{pmatrix} I_1 \\ \vdots \\ \mathrm{I_n} \end{pmatrix}, \tag{7}$$

which can be further simplified as

$$\mathbf{SC} = \mathbf{I}, \tag{8}$$

where $\mathbf{S}$ is an $m \times n$ matrix with the element $S_{mn} = D_n(z_m)$ and $\mathbf{C} = [C_1, C_1, \ldots, C_n]^T$. Generally, it is impossible to obtain an analytical solution of the nonlinear equation like Eq. (8). However, the numerical solution can be easily obtained by the well-developed Newton's theory, which is a powerful tool to approach the exact solution without any search-based optimization algorithm [29]. The detailed implementation of this Newton's theory in combination of the binary-element design can be found in our previous works [48,49].

3. RESULTS

A. Sub-Diffraction Optical Needle

1. 24λ-Long SDON Created by 14-belt BPDOE

First, we design a 24λ-long SDON by using a 14-belt BPDOE, which is exemplified here to show the validity of this approach. The ideal axial intensity is 1 within the expected SDON and 0 beyond the SDON region. The total number of 1 and 0 should be the same as the belt number, so that it yields the only physical solution. A self-made program is carried out in the design that begins with the initial value of 14 width-identical belts and the expected axial intensity profiles. During this task, one round running of program contains 500 iterations, which take only ~30 min in a personal computer [CPU: Intel Core i5-7500 3.4 GHz; RAM: 32G]. Note that when the number of belts is large, the time cost increases due to the increased complexity in Eq. (8). For example, in another design with 27 belts (as shown later), one-round running takes ~3.5 h. After one-round running, the yielded parameters of belts are taken as the initial value of belts for the next-round running; meanwhile, the positions must be modified slightly according to the created intensity profiles so that these predefined locations are close to the physical case. Three rounds are used in this case to finish the design of the BPDOE as shown in Fig. 3(a). The detailed parameters of this BPDOE are shown in Table 1. It creates a 24λ-long SDON, whose simulated intensity profiles are provided in Fig. 3(b). The lateral size evaluated by the full width at its half-maximum (FWHM) of the longitudinal SDON calculated by using RWVD theory is shown in Fig. 3(c). Although the SDON has the lateral size varied along its propagation, the most value is located between the super-oscillation criterion (0.358λ/NA by FWHM) [4,5] and Rayleigh criterion (0.515λ/NA by FWHM), presenting a sub-diffraction feature.

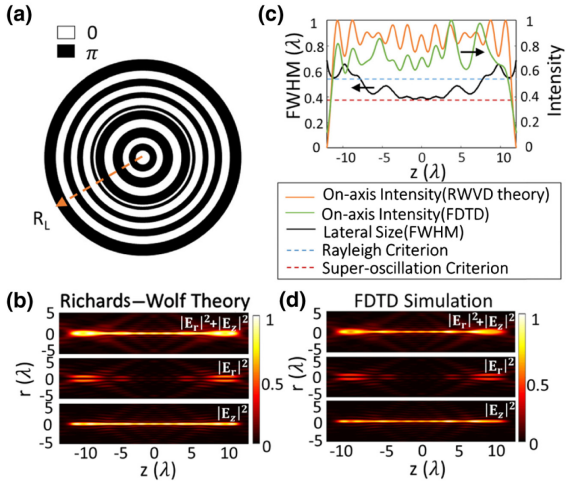

Fig. 3. SDON created by 14-belt BPDOE. (a) The structure diagram of 14-belt BPDOE. The phase of the white and black area is 0 and π, respectively. R_L is the radius of the high-NA lens. (b) The intensity profiles of total (upper), radial (middle), and longitudinal (lower) components according to RWVD theory. (c) Simulated FWHM (left) and intensity profiles (right) of the longitudinal needle. (d) The intensity profiles of total (upper), radial (middle), and longitudinal (lower) components according to FDTD simulation.

2. FDTD Simulation

To doubly check the created SDON, we utilize the finite-difference time-domain (FDTD) method to calculate the intensity profiles of SDON. To implement it, the electromagnetic field at the z-cut plane [with an $x - y$ range of 60λ × 60λ (λ = 632.8 nm in our simulation)] of $z = -15\lambda$ (i.e., 15λ before the focal plane) is calculated by using the RWVD method and then imported into FDTD as the light source. Then the simulation range in the FDTD model is set to 76 μm along the x and y directions [where the perfect match layers (PMLs) are used to suppress the undesired reflection from the boundaries] so that the imported light source can be completely included in the simulation to avoid any numerical error. The simulation range along the z direction with the 12-PML boundaries is set to 19 μm to match the length of the SDON. Due to the large simulation area, the required memory is 85GB, which is available

Table 1. Parameters of the Designed BPDOE

	n	R_n/R_L (where R_L is the radius of the high-NA lens)
10-belt BPDOE	1–10	0.0976, 0.2350, 0.2432, 0.4567, 0.6133, 0.7213, 0.7434, 0.8435, 0.8980, 1
14-belt BPDOE	1–10	0.0714, 0.1434, 0.2050, 0.3081, 0.3931, 0.4809, 0.5010, 0.5338, 0.6096, 0.6687
	11–14	0.7296, 0.8038, 0.8827, 1
27-belt BPDOE	1–10	0.0369, 0.0750, 0.1100, 0.1451, 0.2022, 0.2023, 0.2865, 0.3036, 0.3254, 0.3611
	11–20	0.4144, 0.4647, 0.5093, 0.5370, 0.5790, 0.6025, 0.6424, 0.6754, 0.7265, 0.7477
	21–27	0.7819, 0.8011, 0.8549, 0.8792, 0.9169, 0.9761, 1

in our computer workstation [CPU: Intel Xeon E5-2687W v4 3.00 GHz;RAM: 256G].

The FDTD simulation results [see Fig. 3(d)] of the 24λ-long SDON agree well with the results calculated by RWVD theory. We also plot on-axis intensity profiles of the SDON according to the RWVD theory and the FDTD simulation in Fig. 3(c). It indicates the uniformity of 0.14 and 0.24 [evaluated by $(I_{peak} - I_{valley})/(I_{peak} + I_{valley})$, where I_{peak} and I_{valley} are the maximum peak and minimum valley of the on-axis intensity of the SDON, respectively]. Though the uniformity is worse than that in Refs. [23,50], the optical system with BPDOE and high-NA lens is more practical than that with parabolic mirror [50]; meanwhile, the BPDOE with fewer belts is easier to fabricate than a high-NA Fresnel zone plate [23]. Note that their slight deviation might be caused by the limited-size light source in FDTD and unavoidable simulation error due to the mesh accuracy. In principle, this problem can be solved by using the larger-size light source and the finer meshing grid; however, it requires huge memory in computing.

3. 43λ-Long SDON Created by 27-belt BPDOE

We increase the number of belt up to 27 so that a 43λ-long SDON can be achieved. The design process of the 27-belt BPDOE is the same as that of 14-belt BPDOE. However, the 27-belt design takes more time and requires five rounds, where every round takes around 3.5 h due to the large number of belts. The designed BPDOE has the detailed parameters shown in Table 1 and is sketched in Fig. 4(a). The yielded 43λ-long SDON has the simulated intensity profiles as shown in Fig. 4(b).

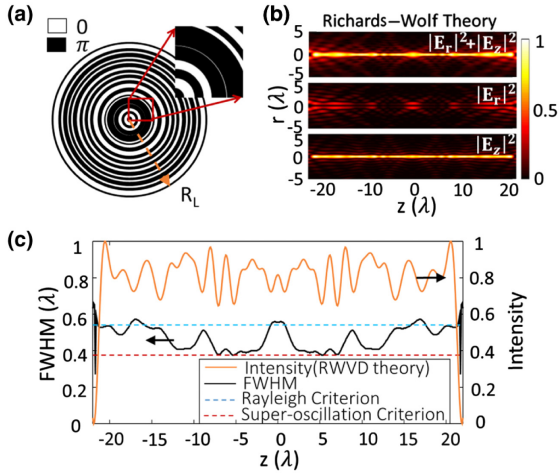

Fig. 4. SDON by 27-belt BPDOE. (a)The structure diagram of 27-belt BPDOE, with partial enlarged view inserted at the upper-right corner. The phase of white and black area is 0 and π, respectively. R_L is the radius of high-NA lens. (b) The intensity profiles of total (upper), radial (middle), and longitudinal (lower) components according to RWVD theory. (c) Simulated FWHM (left) and intensity profiles (right) of the longitudinal needle.

The longitudinal field shows a needle-like distribution with the small intensity variation caused by the constructive interference from light passing through the numerous belts. In Fig. 4(c), the on-axis intensity profile of the SDON indicates the uniformity of 0.21, which is worse than the SDON created by the 14-belt BPDOE. It unveils that modulating optical interference is challenging when the sources involved in the interference process are large. Such a long SDON is too large to carry out the FDTD simulations. In addition, although our approach enables one to achieve the arbitrarily long SDONs in theory, the other performances such as the uniformity in intensity and the lateral size cannot be maintained. It is also possible to use more belts to create the longer SDONs, but the balance between the length of SDON, uniformity, and computation time should be made. Similarly for the uniformity, we can get more uniform SDONs by enlarging the belts of BPDOE but the cost of the computation will increase significantly. Hence, the 27-belt BPDOE is used here after a good balance.

The FWHM of the longitudinal SDON created by the 27-belt BPDOE with the RWVD theory is shown in Fig. 4(c). Around the locations of $z = 0$ (focal plane) and $z = \pm 17\lambda$, the lateral size is above the Rayleigh criterion, which might originate from the reconstructed focus with the imperfect constructive interference that can be doubly observed from the radial component in Fig. 4(b). Interestingly, the needle sizes approach the super-oscillation criterion at the positions of $z = \pm 5.34\lambda$ and $\pm 7\lambda$, but they increase rapidly for any deviation of the axial location. This phenomenon is caused by extremely small depth of focus for a super-oscillatory spot [5]. The lateral sizes of all the reported SDONs (including the ones generated by planar diffractive lenses, reflective mirrors, and a high-NA objective with complex-amplitude modulation) have not broken the super-oscillation criterion of 0.358λ/NA (FWHM), which might suggest a physical limitation to the lateral size of a SDON.

Considering the long-distance propagation without any divergence in this SDON, we calculate its Rayleigh range $z_R = k\tilde{\omega}_0^2/2 = 0.6896\lambda$, where the mean lateral size $\tilde{\omega}_0$ is 0.4685λ within the needle. It indicates that 43λ-long needle has the diffraction-free propagation over a distance of $62.3z_R$, while a 24λ-long needle has only $32.7z_R$, which presents a well-behaved diffraction-free property.

B. Focal Fields with Multiple Hotspots

To explore its capacity, we design the optical field with multiple hotspots by setting a predefined on-axis intensity with the alternative 1 and 0 at the locations of interest. The designed results are provided in Fig. 5, which shows the creation of five hotspots along the propagation by using a 10-belt BPDOE. In this task, the one-round running of the program takes ∼ 11 min, and five rounds are also needed to finalize the design. The dimensions of this 10-belt BPDOE are shown in Table 1 and sketched in Fig. 5(a). The simulated intensity profiles reveal that every longitudinally polarized spot is uniform and discrete, while the coexistence of the radial component makes the total field behave like optical hollow cage as shown in Fig. 5(b). Fortunately, the null on-axis intensity of the radial component has no influence on the axial intensity of the total field as shown in Fig. 5(c), which indicates the uniformity calculated by RWVD and FDTD is 0 and 0.12 [evaluated by $(I_{\text{maxpeak}} - I_{\text{minpeak}})/(I_{\text{maxpeak}} + I_{\text{minpeak}})$, where I_{maxpeak} and I_{minpeak} are the maximum and minimum of the multiple hotspots, respectively]. Similarly, we use the FDTD method to check the simulated multiple hotspots. The simulated results in FDTD have good agreement with the RWVD theory as illustrated in Figs. 5(c) and 5(d). However, the radial component with the doughnut-shape cross section increases the lateral sizes of all the hotspots as observed in Fig. 5(e). In comparison, the longitudinal component yields the sub-diffraction hotspots, each of which has the axial length of ∼1.5λ (FWHM).

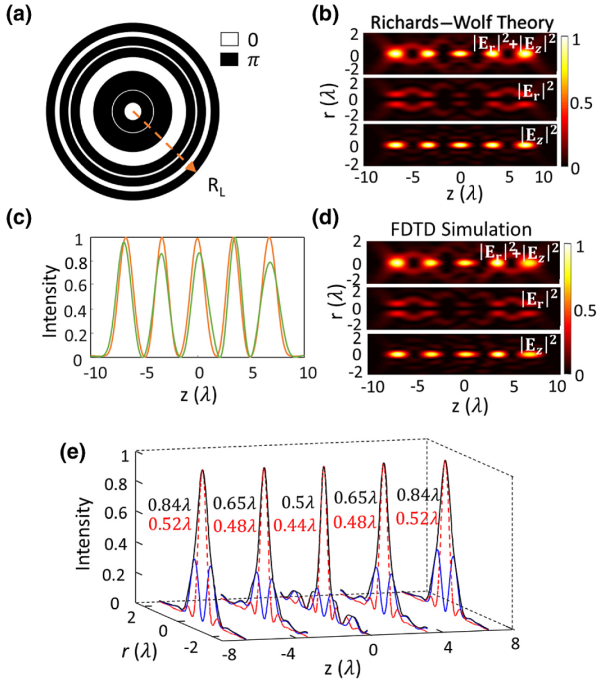

Fig. 5. Multiple hotspots created by 10-belt BPDOE. (a) The structure diagram of the designed 10-belt BPDOE to create the hotspots. The phase of white and black area is 0 and π, respectively. R_L is the radius of high-NA lens. (b) The simulated fields for total (upper), radial (middle), and longitudinal (lower) components according to RWVD theory. (c) The on-axis intensity distribution of multiple hotspots according to RWVD theory (orange) and FDTD simulation (green). (d) The simulated fields for total (upper), radial (middle), and longitudinal (lower) components according to FDTD simulation. (e) The lateral intensity of radial (blue solid curve), longitudinal (red dashed curve), and total (dark solid curve) field for each focal spot. The inserted numbers are the FWHMs of total (black) and longitudinal (red) field components.

4. DISCUSSION

Although another method to reverse the radiation from a dipole array [51] or uniform line source [52] can be used to create the optical needles, the yielded elements must take the complex-amplitude modulation, which increases the experimental difficulty compared with the pure binary amplitude or phase elements. Therefore, our optimization-free method has threefold advantages. First, it offers an easier way to customize the required focal fields with the predefined intensity profiles at the arbitrary locations, so a record-long SDON is achieved in comparison with other results in the same configuration. Second, the designed pure-phase elements do not bring any energy loss in principle, which thus allows high efficiency. In addition, the BPDOE can be fabricated easily by using electron-beam lithography (EBL) or focused ion beam (FIB) lithography due to the only binary phase modulation. Third, it yields a physical solution for a predefined intensity at a given position, which helps us to find the low-cost design.

Although our optimization-free method is merely focused on the on-axis intensity of the expected fields, the other parameters such as the lateral size, Strehl ratio, and the sidebands of the spot are also kept well. In fact, it is contributed to the way we set the expected on-axis intensity. Namely, optical needle or hotspots have the on-axis intensity of 1, while the on-axis intensity beyond the region of interest is 0. Such an on-axis intensity indicates that the constructive interference must happen at the interested region (i.e., needles or hotspots), but the destructive interference is needed at the zero on-axis intensity. Therefore, the spot with constructive interference will definitely carry the small lateral size, good Strehl ratio, and low sidebands.

Some other issues about the design of BPDOE are also clarified. Firstly, one cannot obtain the exact solution of the nonlinear Eq. (8), even using advanced Newton's theory. Within every iteration, the yielded solution is only the approximate solution, which depends tightly on the predefined on-axis intensity profiles. Secondly, the solution provided by our optimization-free method depends on the initial value. The initial $\mathbf{R_n}$ $(R_n = [\frac{1}{N}, \frac{2}{N}, \ldots, \frac{n}{N}, \ldots, 1] \cdot R_L$, where N in number of total belts, n is the nth belt, and R_L is the radius of BPDOE) with equal interval is used in our design. Once the initial $\mathbf{R_n}$ changes, one will obtain the different solutions. But these solutions have no big difference because all of them approach the expected solution closely.

5. CONCLUSION

In conclusion, we have proposed an optimization-free method to design a BPDOE that is combined with a high-NA lens to focus the radially polarized light for customization of optical focal fields. The described inverse problem in terms of a nonlinear matrix equation enables the design of BPDOE without traditional search-based optimization. The 43λ-long longitudinally polarized needle without any divergence is created by phase modulation of a 27-belt BPDOE. The trade-off among the length, the uniformity, and lateral size of optical needle should be made to obtain a physical solution for practical applications. The universality of this method is verified by designing uniform sub-diffraction hotspots with a 10-belt BPDOE, which might be applied in optical micro-manipulation, nano-imaging, and lithography.

Funding. National Natural Science Foundation of China (61875181); USTC Research Funds of the Double First-Class Initiative (YD2030002003); CAS Pioneer Hundred Talents Program; Natural Science Foundation of Anhui Province (1808085QF199).

Acknowledgment. K. H. acknowledges the support from the University of Science and Technology of China's Centre for Micro and Nanoscale Research and Fabrication.

Disclosures. The authors declare no conflicts of interest.

Data Availability. Data underlying the results presented in this paper are not publicly available at this time but may be obtained from the authors upon reasonable request.

REFERENCES

1. D. Lu and Z. Liu, "Hyperlenses and metalenses for far-field super-resolution imaging," Nat. Commun. **3**, 1205 (2012).
2. Z. Gan, Y. Cao, R. A. Evans, and M. Gu, "Three-dimensional deep sub-diffraction optical beam lithography with 9 nm feature size," Nat. Commun. **4**, 2061 (2013).
3. N. I. Zheludev, "What diffraction limit?" Nat. Mater. **7**, 420–422 (2008).
4. F. Qin, K. Huang, J. Wu, J. Teng, C. W. Qiu, and M. Hong, "A supercritical lens optical label-free microscopy: sub-diffraction resolution and ultra-long working distance," Adv. Mater. **29**, 1602721 (2017).
5. K. Huang, F. Qin, H. Liu, H. Ye, C. W. Qiu, M. Hong, B. Luk'yanchuk, and J. Teng, "Planar diffractive lenses: fundamentals, functionalities, and applications," Adv. Mater. **30**, 1704556 (2018).
6. S. Xue, Q. Liu, T. Liu, S. Yang, P. Su, K. Liu, B. Tian, and T. Wang, "Electromagnetic exploration of focusing properties of high-numerical-aperture micro-Fresnel zone plates," Opt. Commun. **426**, 41–45 (2018).
7. E. T. F. Rogers, S. Savo, J. Lindberg, T. Roy, M. R. Dennis, and N. I. Zheludev, "Super-oscillatory optical needle," Appl. Phys. Lett. **102**, 031108 (2013).
8. G. Yuan, E. T. F. Rogers, T. Roy, G. Adamo, Z. Shen, and N. Zheludev, "Planar super-oscillatory lens for sub-diffraction optical needles at violet wavelengths," Sci. Rep. **4**, 6333 (2014).
9. F. Qin, K. Huang, J. Wu, J. Jiao, X. Luo, C. Qiu, and M. Hong, "Shaping a subwavelength needle with ultra-long focal length by focusing azimuthally polarized light," Sci. Rep. **5**, 09977 (2015).
10. D. Panneton, G. St-Onge, M. Piche, and S. Thibault, "Needles of light produced with a spherical mirror," Opt. Lett. **40**, 419–422 (2015).
11. H. Dehez, A. April, and M. Piche, "Needles of longitudinally polarized light: guidelines for minimum spot size and tunable axial extent," Opt. Express **20**, 14891–14905 (2012).
12. M. Zhu, Q. Cao, and H. Gao, "Creation of a 50,000λ long needle-like field with 0.36λ width," J. Opt. Soc. Am. **31**, 500–504 (2014).
13. K. Huang, P. Shi, X.-L. Kang, X. Zhang, and Y.-P. Li, "Design of DOE for generating a needle of a strong longitudinally polarized field," Opt. Lett. **35**, 965–967 (2010).
14. C. C. Sun and C. K. Liu, "Ultrasmall focusing spot with a long depth of focus based on polarization and phase modulation," Opt. Lett. **28**, 99–101 (2003).
15. H. Wang, S. Lupingshi, B. Lukyanchuk, C. Sheppard, and C. T. Chong, "Creation of a needle of longitudinally polarized light in vacuum using binary optics," Nat. Photonics **2**, 501–505 (2008).
16. T. Zhang, M. Li, H. Ye, and C. Shi, "Ultra-long and high uniform optical needle generated with genetic algorithm based multifocal positions optimization," Opt. Commun. **460**, 125178 (2020).
17. J. Lin, K. Yin, Y. Li, and J. Tan, "Achievement of longitudinally polarized focusing with long focal depth by amplitude modulation," Opt. Lett. **36**, 1185–1187 (2011).
18. T. Liu, J. Tan, J. Liu, and J. Lin, "Creation of subwavelength light needle, equidistant multi-focus, and uniform light tunnel," J. Mod. Opt. **60**, 378–381 (2013).
19. J. Guan, J. Lin, C. Chen, Y. Ma, J. Tan, and P. Jin, "Transversely polarized sub-diffraction optical needle with ultra-long depth of focus," Opt. Commun. **404**, 118–123 (2017).
20. K. Hu, Z. Chen, and J. Pu, "Generation of super-length optical needle by focusing hybridly polarized vector beams through a dielectric interface," Opt. Lett. **37**, 3303–3305 (2012).
21. Z. Man, C. Min, L. Du, Y. Zhang, S. Zhu, and X. Yuan, "Sub-wavelength sized transversely polarized optical needle with exceptionally suppressed side-lobes," Opt. Express **24**, 874–882 (2016).
22. L. Turquet, X. Zang, J. P. Kakko, H. Lipsanen, G. Bautista, and M. Kauranen, "Demonstration of longitudinally polarized optical needles," Opt. Express **26**, 27572–27584 (2018).
23. T. Liu, J. Tan, J. Liu, and H. Wang, "Modulation of a super-Gaussian optical needle with high-NA Fresnel zone plate," Opt. Lett. **38**, 2742–2745 (2013).
24. Y. Zha, J. Wei, H. Wang, and F. Gan, "Creation of an ultra-long depth of focus super-resolution longitudinally polarized beam with a ternary optical element," J. Opt. **15**, 075703 (2013).
25. S. Liu, Z. Guo, P. Li, B. Wei, and J. Zhao, "Tightly autofocusing beams: an effective enhancement of longitudinally polarized fields," Opt. Lett. **45**, 575–578 (2020).
26. Z. X. Fang, Y. X. Ren, L. Gong, P. Vaveliuk, Y. Chen, and R. D. Lu, "Shaping symmetric Airy beam through binary amplitude modulation for ultralong needle focus," J. Appl. Phys. **118**, 203102 (2015).
27. Z. Nie, G. Shi, X. Zhang, Y. Wang, and Y. Song, "Generation of super-resolution longitudinally polarized beam with ultra-long depth of focus using radially polarized hollow Gaussian beam," Opt. Commun. **331**, 87–93 (2014).
28. H. Ye, K. Huang, H. Liu, F. Wen, Z. Jin, J. Teng, and C. W. Qiu, "Intrinsically shaping the focal behavior with multi-ring Bessel-Gaussian beam," Appl. Phys. Lett. **111**, 031103 (2017).
29. J. B. Schneider, *Understanding the Finite-Difference Time-Domain Method* (2017).
30. Q. Zhan, "Cylindrical vector beams: from mathematical concepts to applications," Adv. Opt. Photon. **1**, 1–57 (2009).
31. K. Huang, P. Shi, G. W. Cao, K. Li, X. B. Zhang, and Y. P. Li, "Vector-vortex Bessel-Gauss beams and their tightly focusing properties," Opt. Lett. **36**, 888–890 (2011).
32. X.-L. Wang, J. Ding, W.-J. Ni, C.-S. Guo, and H.-T. Wang, "Generation of arbitrary vector beams with a spatial light modulator and a common path interferometric arrangement," Opt. Lett. **32**, 3549–3551 (2007).
33. S. Liu, P. Li, T. Peng, and J. Zhao, "Generation of arbitrary spatially variant polarization beams with a trapezoid Sagnac interferometer," Opt. Express **20**, 21715–21721 (2012).
34. K. S. Youngworth and T. G. Brown, "Focusing of high numerical aperture cylindrical vector beams," Opt. Express **7**, 77–87 (2000).
35. D. P. Biss, K. S. Youngworth, and T. G. Brown, "Dark-field imaging with cylindrical-vector beams," Appl. Opt. **45**, 470–479 (2006).
36. X.-L. Wang, J. Chen, Y. Li, J. Ding, C.-S. Guo, and H.-T. Wang, "Optical orbital angular momentum from the curl of polarization," Phys. Rev. Lett. **105**, 253602 (2010).
37. G. Milione, H. I. Sztul, D. A. Nolan, and R. R. Alfano, "Higher-order Poincaré sphere, Stokes parameters, and the angular momentum of light," Phys. Rev. Lett. **107**, 053601 (2011).

38. X. Hao, C. Kuang, T. Wang, and X. Liu, "Phase encoding for sharper focus of the azimuthally polarized beam," Opt. Lett. **35**, 3928–3930 (2010).
39. S. Wang, X. Li, J. Zhou, and M. Gu, "Ultralong pure longitudinal magnetization needle induced by annular vortex binary optics," Opt. Lett. **39**, 5022–5025 (2014).
40. X.-Z. Gao, P.-C. Zhao, X.-F. Sun, F. Yang, Y. Pan, Y. Li, C. Tu, and H.-T. Wang, "Highly purified transversely polarized optical needle generated by the hybridly polarized vector optical field with hyperbolic symmetry," J. Opt. **22**, 105604 (2020).
41. Y. Zhao, Q. Zhan, Y. Zhang, and Y.-P. Li, "Creation of a three-dimensional optical chain for controllable particle delivery," Opt. Lett. **30**, 848–850 (2005).
42. L. Cicchitelli, H. Hora, and R. Postle, "Longitudinal field components for laser beams in vacuum," Phys. Rev. A **41**, 3727 (1990).
43. D. P. Biss and T. G. Brown, "Polarization-vortex-driven second-harmonic generation," Opt. Lett. **28**, 923–925 (2003).
44. A. Bouhelier, M. Beversluis, A. Hartschuh, and L. Novotny, "Near-field second-harmonic generation induced by local field enhancement," Phys. Rev. Lett. **90**, 013903 (2003).
45. N. Hayazawa, Y. Saito, and S. Kawata, "Detection and characterization of longitudinal field for tip-enhanced Raman spectroscopy," Appl. Phys. Lett. **85**, 6239–6241 (2004).
46. M. Xiao, "Theoretical treatment for scattering scanning near-field optical microscopy," J. Opt. Soc. Am. A **14**, 2977–2984 (1997).
47. B. Richards and E. Wolf, "Electromagnetic diffraction in optical systems," Proc. R. Soc. London A **253**, 358–379 (1959).
48. K. Huang, H. Ye, J. Teng, S. P. Yeo, B. Luk'yanchuk, and C. W. Qiu, "Optimization-free superoscillatory lens using phase and amplitude masks," Laser Photon. Rev. **8**, 152–157 (2014).
49. C. Wan, K. Huang, T. Han, E. S. P. Leong, W. Ding, L. Zhang, T.-S. Yeo, X. Yu, J. Teng, D. Y. Lei, S. A. Maier, B. Luk'yanchuk, S. Zhang, and C. W. Qiu, "Three-dimensional visible-light capsule enclosing perfect supersized darkness via antiresolution," Laser Photon. Rev. **8**, 743–749 (2014).
50. T. Liu, J. Tan, J. Lin, and J. Liu, "Generating super-Gaussian light needle of 0.36λ beam size and pure longitudinal polarization," Opt. Eng. **52**, 074104 (2013).
51. J. Wang, W. Chen, and Q. Zhan, "Engineering of high purity ultra-long optical needle field through reversing the electric dipole array radiation," Opt. Express **18**, 21965–21972 (2010).
52. Y. Yu and Q. Zhan, "Optimization-free optical focal field engineering through reversing the radiation pattern from a uniform line source," Opt. Express **23**, 7527–7534 (2015).